

Impurity effects on the intergranular liquid bismuth penetration in polycrystalline nickel

Kaveh Meshinchi Asl, Jian Luo *

School of Materials Science and Engineering, Center for Optical Materials Science and Engineering Technologies, Clemson University, Clemson, SC 20634, USA

Received 19 August 2011; received in revised form 18 September 2011; accepted 21 September 2011

Abstract

The effects of impurities on the intergranular penetration of Bi based liquids in polycrystalline Ni at 700 °C were systematically investigated. In comparison with a nominally pure Ni (99.9945%), the presence of a total amount of <0.5 at.% impurities of Mn, Fe and Si in the Ni increased the penetration length by six times when a near-equilibrium Bi–Ni liquid was applied; when an initially pure Bi liquid was applied, this increment further enlarged to ~20 times in the initial penetration stage. In a second set of controlled experiments, the addition of Mn, Sn and Fe to the liquid Bi–Ni all enhanced the intergranular penetration, but produced different kinetics and morphologies. We extended a concept that was initially proposed in the Rice–Wang model for grain boundary embrittlement to explain our observations of the impurity-enhanced intergranular penetration based on a theory that segregation of an impurity could reduce the grain boundary energy more rapidly than the solid–liquid interfacial energy. Correspondingly, a new analytical model for the effect of adding a third impurity on changing the equilibrium dihedral angle and the associated intergranular penetration kinetics has been derived for the dilute solution limit. Furthermore, we demonstrated that the interplay of bulk phase equilibria, interfacial segregation, transport (dissolution, precipitation and diffusion) processes and stress generation could effectively explain a variety of different intergranular penetration behaviors and morphologies that have been observed in the experiments conducted using 10 different combinations of the solid and liquid metals. The framework for understanding the impurity effects on intergranular liquid penetration developed in this study can be applied to other materials systems. This study has practical importance for understanding and controlling liquid metal corrosion and embrittlement.

© 2011 Acta Materialia Inc. Published by Elsevier Ltd. All rights reserved.

Keywords: Grain boundary; Wetting; Liquid metal corrosion; Liquid metal embrittlement

1. Introduction

The chemical and mechanical stabilities of polycrystalline solid metals in contact with liquid metals are important for understanding and controlling hot dip galvanization, welding, soldering and other materials processes [1–13]. Compatibilities of solid and liquid metals are especially important for the safe usages of liquid metals in the cooling circuits in nuclear reactors, as well as in spallation target-based nuclear energy generation and nuclear waste incineration systems [1–9,13]. Specifically, when polycrystalline

solids are in contact with certain liquids, deep grain boundary (GB) grooves can develop and liquids can quickly penetrate into the GBs. This has been studied in the context of two related, technologically important, materials phenomena: liquid metal corrosion [5–9,13] and liquid metal embrittlement [1–4,10–12,14–16].

On the one hand, liquid metal corrosion studies focus on the dissolution at the solid–liquid interfaces. When polycrystalline solids metals are used, preferential intergranular dissolution and penetration are the dominant corrosion processes in many systems. Recently, there has been an increasing number of studies of liquid metal corrosion owing to their applications in nuclear reactors, and these have been documented in several review articles [5–7,13]. However,

* Corresponding author. Tel.: +1 864 656 5961; fax: +1 864 656 1453.
E-mail address: jluo@alum.mit.edu (J. Luo).

most of the prior studies were focused on the macroscopic level; little work has been conducted to investigate the microstructural aspects. In particular, the intergranular penetration and its controlling factors are not understood. We recognize that the impurity effects on liquid metal corrosion have been investigated in the context of seeking corrosion inhibitors, particularly for the system of steels in contact with the Pb–Bi liquid, because of their applications in advanced nuclear reactors. It was proposed that the addition of Zr and Ti can significantly inhibit the liquid metal corrosion of carbon steels and low-alloy steels, but it does not have much effect on the stainless steels [5–7,17]. However, we should point out that these corrosion inhibitors prevent the dissolution of solids by promoting the formation of protective oxide layers on the solid surfaces. This study is focused on the impurity effect of intergranular penetration without surface native oxide layers (where surface oxide layers were removed prior to intergranular penetration experiments). To the best of our knowledge, despite it being practically important in part because it represents the late stage of corrosion after breaking the native oxides [13], no such study been systematically conducted before.

On the other hand, the intergranular penetration in Ni–Bi, Cu–Bi and Al–Ga binary systems (where the primary/solid phases are underlined) has been investigated in the context of liquid metal embrittlement [1–3,10–12,14,15], where the intergranular penetration and the adsorption of the liquid metal species at the GBs in front of the penetration tips can cause brittle intergranular fracture at unusually low stress levels. Most of these studies have been conducted for binary systems only. The effects of adding a third impurity have not been systematically assessed, and this motivated our study.

Investigating the impurity effects on intergranular penetration is important for at least two reasons. First, engineering materials are rarely used as their pure form. The presence of impurities or internally added alloying elements prevails in most structural metals as well as liquid metals. Second, understanding the impurity effects can offer a way to intentionally control the intergranular penetration, as well as the related corrosion and embrittlement.

In this study, we selected Ni–Bi as the model system. We demonstrate – for the first time to our knowledge – significant enhancements in intergranular liquid metal penetration upon adding small amounts of impurities in either the solid phase or the liquid. Furthermore, we propose a general framework to explain such impurity effects on intergranular liquid penetration; specifically, we derive a new analytical model for the impurity effect for the dilute solution limit, and we further systematically demonstrate how the interplay of the bulk phase equilibria, interfacial segregation, diffusion, dissolution, precipitation and stress generation can result in a variety of different intergranular penetration behaviors and morphologies. These new findings, as well as the model and framework developed in this study, are generally useful for

understanding and controlling liquid metal corrosion and embrittlement phenomena.

Recent studies have suggested that GBs can be considered as discrete interfacial phases [18–24], and a series of generic GB phases (also called “complexions”) have been discovered experimentally [18–21,25–29]. In particular, a bilayer interfacial phase, which was hidden in prior studies because it is not clearly discernible under conventional high-resolution transmission electron microscopy, was recently observed at the general (large-angle, low-symmetry, random) GBs in the Ni–Bi binary system by aberration-corrected, high-angle annular dark-field (HAADF) scanning transmission electron microscopy (STEM) [30]. In general, the formation of interfacial phases can drastically change the microstructural evolution and materials properties [18–21,25,29,31,32]. Specifically, a series of studies have been conducted to probe GB phase formation and their implications in metallic alloys [29–39]. The present study demonstrates the significant effects that the addition of a relatively minor amount of a third impurity has on the GB/interface controlled intergranular penetration, and it could motivate future investigations to characterize the underlying atomic-scale interfacial structures and to probe possible interfacial phase behaviors.

2. Experimental procedure

Polycrystalline Ni foils with nominal purities of 99.9945 and 99.5% (atomic percentages) were purchased from Alfa Aesar Company. They are referred to as to “pure” and “impure” Ni, respectively, in the following text. The main impurities in the impure (99.5%) Ni foils are Mn (0.21 at.%), Fe (0.14 at.%) and Si (0.1 at.%). The as-received pure and impure Ni foils had initial average grain sizes of 75 and 25 μm , respectively; the impure foils were then annealed at 900 °C for 2 h to obtain an average grain size of $\sim 75 \mu\text{m}$, to be comparable to that of pure Ni foils. All Ni foils were ground with silicon carbide lapping films (up to 1200 grits), fine polished with 1.0 and 0.3 μm alumina suspensions, and cleaned in pure acetone. The polished side of the Ni foils was put in contact with the Bi powders or (pre-made) 1Bi–0.36Ni alloy beads in an alumina boat. The 1Bi–0.36Ni alloy (i.e. 73.5 at.% Bi + 26.5 at.% Ni; for simple comparisons, we usually use atomic ratios to label the starting liquid/alloy compositions and normalize the ratios to 1Bi), which has an equilibrium liquidus composition at 700 °C based on the Ni–Bi phase diagram [40], was made and used in most penetration experiments to avoid dissolution of the Ni from the solid foils into the liquids. The alumina boat was placed in a horizontal tube furnace in a flow of a forming gas (95 mol.% Ar + 5 mol.% H₂). Ti sponges were used as a getter to help to remove/reduce the remaining oxygen and moisture.

To investigate the effects of impurities in the melts, Mn, Sn and Fe were individually added to the 1Bi–0.36Ni alloy (liquid metals at 700 °C). Two sets of Bi–Ni–*M* (*M* = Mn, Sn or Fe) alloys were made. In the first set, 1 at.% of *M* was

added to 1Bi–0.36Ni alloys to attain the composition of 1Bi–0.36Ni–0.014M. In the second set, 5 wt.% of M was added to 1Bi–0.36Ni alloys to attain the compositions of 1Bi–0.36Ni–0.21Mn, 1Bi–0.35Ni–0.10Sn and 1Bi–0.36Ni–0.21Fe, respectively (i.e. 13.3 at.% Mn, 6.7 at.% Sn and 13.1 at.% Fe, respectively, in the alloys). These pre-made ternary Ni–Bi–M alloy beads were also placed on the top of the polished Ni foils to conduct isothermal penetration experiments to examine the effects of impurities when they were added in the starting liquids.

All specimens were annealed at 700 °C for various durations, then quenched in water to preserve the high-temperature structures. Note that most of our binary (Ni–Bi) and ternary (Ni–Bi–M) systems exhibit only two equilibrium bulk phases upon annealing of 700 °C: an Ni-rich solid body-centered cubic phase and a Bi-rich liquid phase; the only exception is that, with the addition of 5 wt.% Sn, a third phase (Ni₃Sn) was precipitated. Quenched specimens were cut transversely and the cross-sectional specimens were examined using a Hitachi SU6600 field-emission scanning electron microscope (SEM) equipped with an energy-dispersive X-ray (EDX) spectroscopy analyzer.

3. Results

3.1. The Ni–Bi binary system

Direct exposure of a solid pure (99.9945%) Ni to an equilibrium Bi–0.36Ni liquid resulted in the formation of grooves and liquid penetration along the GBs of the pure Ni. In this experiment, the starting liquid (Bi–0.36Ni) was in chemical equilibrium with Ni (noting that the solid Ni phase has virtually no solubility of Bi); thus there was no overall dissolution of Ni into the Bi-rich liquid during the annealing. Fig. 1a shows a cross-section of a typical groove formed in a sample that was annealed at 700 °C for 5 h and quenched. The dihedral angles (θ) were measured individually, and the distribution of the measured dihedral angles for the specimen annealed at the 700 °C for 5 h is shown in Fig. 1b. The average dihedral angle was measured to be 44.7° and the corresponding standard deviation was 19.6°. Presumably, the boundary-to-boundary variations were related to the different crystallographies of the individual GBs. Moreover, the measured dihedral angles were two-dimensional (2-D) projections of the true 3-D dihedral

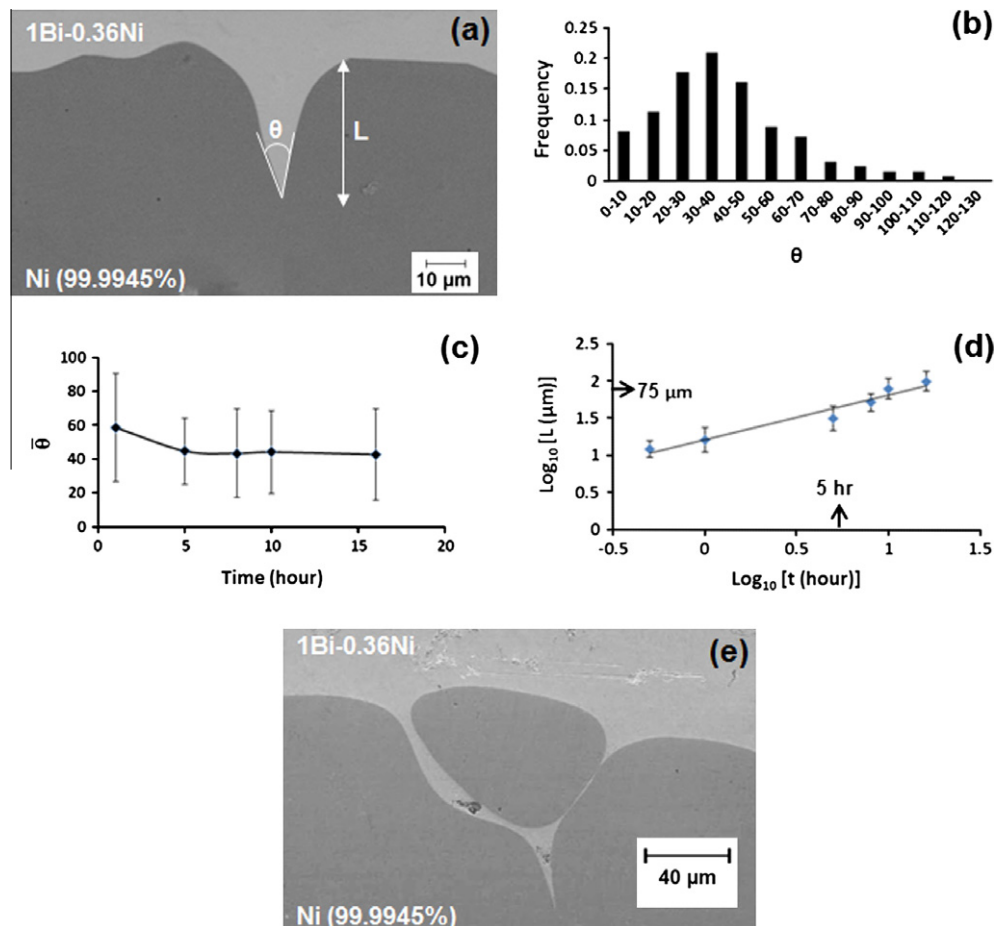


Fig. 1. Summary of the results of the intergranular penetration of the equilibrium Bi–Ni liquid in pure Ni at 700 °C. (a) A cross-sectional SEM micrograph of a typical GB groove after annealing for 5 h. L is the penetration length and θ is the dihedral angle at the penetration tip. (b) The distribution of measured dihedral angles at different GBs in this specimen. (c) Measured average dihedral angle and (d) penetration length vs. annealing time. (e) In a specimen that was annealed at 700 °C for 16 h, the liquid penetration length exceeded the grain size.

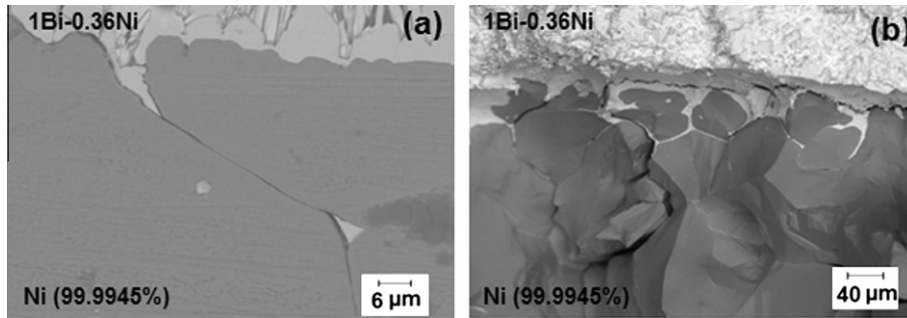


Fig. 2. Intergranular fractures were evident in the SEM micrographs of the (a) cross-sectional and (b) fracture surfaces.

Table 1

Summary of the measured penetration length (mean \pm 1 standard deviation, μm) for experiments performed under various conditions.

Solid Ni	Starting liquid composition	Annealing time					
		0.5 h	1 h	5 h	8 h	10 h	16 h
“Pure” 99.9945% Ni	1Bi–0.36Ni	9 \pm 4	16 \pm 7	31 \pm 15	51 \pm 14	77 \pm 22	97 \pm 34
	Pure Bi	9.5 \pm 5		38 \pm 17			
	1Bi–0.36Ni–0.014Mn			95 \pm 14			
	1Bi–0.36Ni–0.21Mn	264 \pm 18		524 \pm 63			
	1Bi–0.36Ni–0.014Sn			338 \pm 19			
	1Bi–0.35Ni–0.10Sn			380 \pm 27			
	1Bi–0.36Ni–0.014Fe			292 \pm 18			
	1Bi–0.36Ni–0.21Fe			337 \pm 48			
“Impure” 99.5% Ni 0.21% Mn 0.14% Fe 0.1% Si	1Bi–0.36Ni			176 \pm 18			
	Pure Bi	187 \pm 7		>200			

angles, producing further variations; however, the average dihedral angles measured in 2-D cross-sections should theoretically be identical to the average dihedral angle in three dimensions after making a significant number of measurements [41]. Fig. 1c indicates that after approximately 5 h the average dihedral angle reached a steady state. We also measured the average liquid penetration length (L) as a function of time (Fig. 1d). After \sim 5 h, the liquid penetration length exceeded the Ni grain size (Fig. 1e). Intergranular fractures were often evident (Fig. 2), indicating GBs were embrittled. It was well established that the adsorption of Bi at Ni GBs in front of the penetration tips embrittled the GBs, a phenomenon known as “liquid metal embrittlement” [2,4,10,11].

In an additional experiment, we used the initially pure Bi liquid to penetrate the polycrystalline pure (99.9945%) Ni at the same temperature. Here, there should be a net dissolution of Ni into the Bi-rich liquid in the initial stage of annealing until the liquid composition reached the equilibrium (1Bi–0.36Ni). EDX analysis of the water-quenched specimens showed that the liquid had reached the equilibrium composition on the liquidus line at 700 °C (i.e. 1Bi–0.36Ni or 73.5 at.% Bi + 26.5 at.% Ni) after 5 h. The average dihedral angle was measured to be $41.3 \pm 17.8^\circ$, which was roughly the same as the measured average dihedral angle when the equilibrium 1Bi–0.36Ni was used as the starting liquid ($44.7 \pm 19.6^\circ$). This again suggested that dissolution was completed and a chemical equilibrium was reached after 5 h (even if the starting liquid was pure Bi).

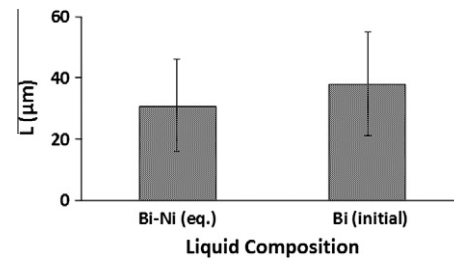


Fig. 3. Comparison of the intergranular penetration lengths (L s) when pure Ni foils were annealed in contact with an equilibrium 1Bi–0.36Ni liquid and an initially pure Bi liquid, respectively, at 700 °C for 5 h.

The average penetration lengths after annealing for 5 h were measured to be 31 and 38 μm when the starting liquid was 1Bi–0.36Ni and pure Bi, respectively (Table 1 and Fig. 3). The slight increase in penetration length when pure Bi was used as the starting liquid can be attributed to the dissolution effect.

3.2. Impurities in the solid Ni

Fig. 4 shows a comparison of the intergranular penetration of the equilibrium 1Bi–0.36Ni liquid in pure (99.9945%) and impure (99.5%) Ni. Specifically, the cross-sectional SEM images of intergranular liquid penetration of pure and impure specimens of similar grain size after annealing for 5 h are shown in Fig. 4a vs. c, respectively; here, the presence of \sim 0.5 at.% impurities

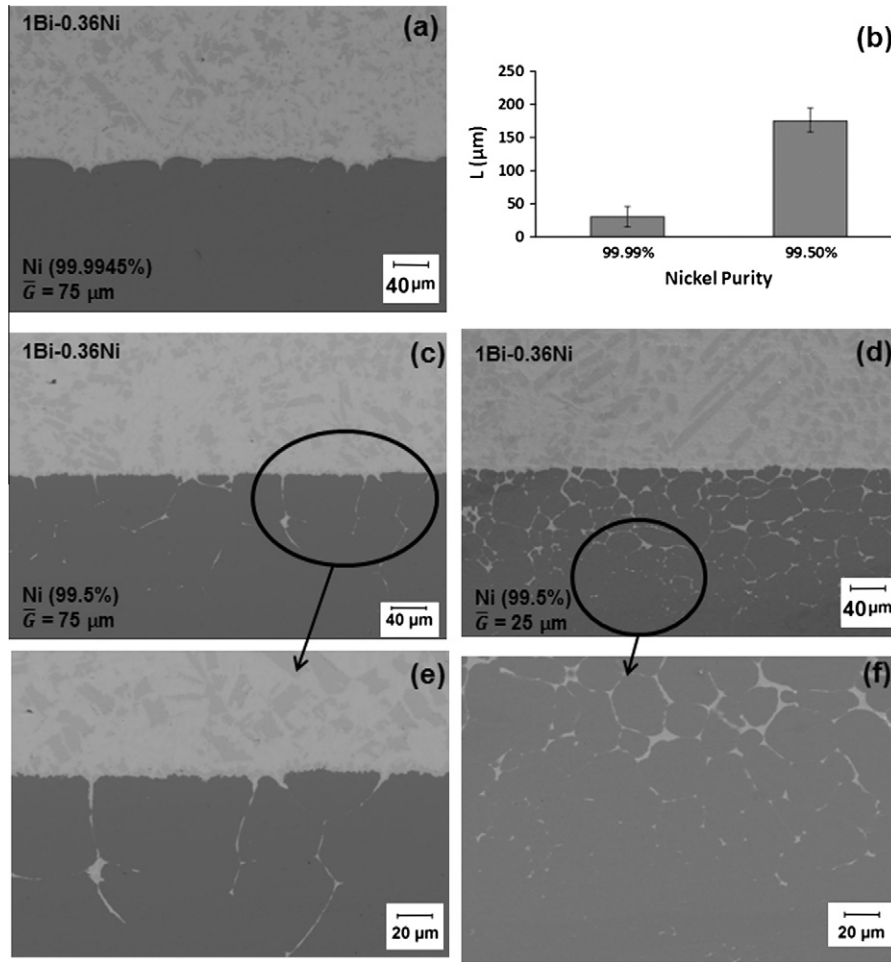


Fig. 4. The intergranular penetration of the equilibrium Bi–Ni liquid was significantly faster in (c) an impure Ni specimen (99.5% Ni, 0.21% Mn, 0.14% Fe and 0.1% Si) than that in (a) a pure (99.9945%) Ni specimen of a similar grain size. (b) The measured average penetration lengths for cases (a) vs. (c). (d) The intergranular penetration of the equilibrium Bi–Ni liquid in an impure specimen of a smaller average grain size. (e) and (f) Enlarged images of the circled area of panels (c) and (d), respectively. In all cases, the Ni specimens were brought into contact with equilibrium 1Bi–0.36Ni liquids and annealed at 700 °C for 5 h.

(0.21 at.% Mn, 0.14 at.% Fe and 0.1 at.% Si) in the Ni solid resulted in a 6-fold increase in the average liquid penetration length (Fig. 4b). At the same time, the average dihedral angle decreased significantly, from 44.7 to $\sim 5^\circ$ ($<10^\circ$ generally; Fig. 5); however, accurate measurements of the dihedral angle in the impure specimens were difficult because of the frequent breaking up of the thin liquid tips during cooling/solidification and the further smearing of Bi by the electron beam irradiation in the SEM (Fig. 5). The similar impurity enhancement effect was also evident in an impure Ni with a smaller grain size (Fig. 4d and f).

When the pure Bi was used as the starting liquid, this impurity effect of enhancing penetration was even more pronounced, as vividly demonstrated in Fig. 6a vs. b. This effect was particularly significant in the initial stage, when Ni was dissolving into the liquid. The average penetration lengths after annealing for 0.5 h in the 99.9945 and 99.5 at.% Ni foils were measured to be 9.5 and 187 μm , respectively (Table 1); this represents an ~ 20 -fold increase (Fig. 6c), which is in contrast to the observation that apply-

ing initially pure Bi (vs. an equilibrium 1Bi–0.36Ni liquid) increased the penetration length in the pure Ni by only $\sim 23\%$ (Fig. 3).

The evolution of liquid penetration as a function of time in the impure Ni foil is shown in Fig. 7. As shown in Fig. 7b–d, the apparent dihedral angle decreased from 44.7° (in 99.9945% Ni) to $<10^\circ$ (in 99.5% Ni), though the exact angle could not be measured accurately because the very thin Bi penetration tips broke during solidification (Fig. 7c and d). The widths of the channels increased with increasing annealing time (Figs. 6a and 7e and f), and this increase was more significant in the early stage (Fig. 7a vs. e). This was presumably related to the dissolution of Ni, which will be discussed further in Section 4.4.

3.3. Impurities in the Ni–Bi liquid

In a second set of controlled experiments, we added Fe, Mn and Sn (separately) into the 1Bi–0.36Ni liquid. As shown in Fig. 8, the addition of these impurities into the

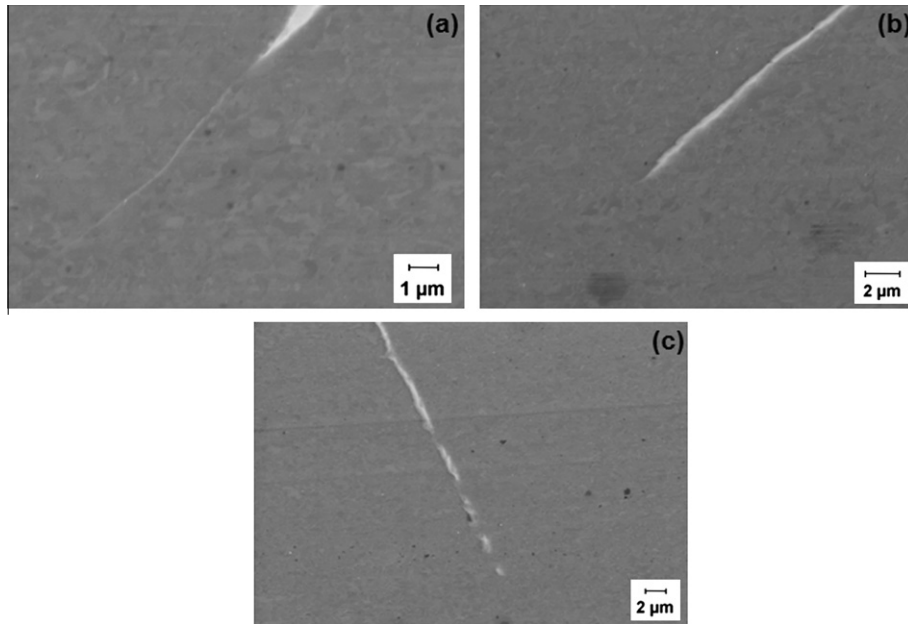


Fig. 5. Representative images of the tips of the intergranular penetration of the equilibrium Bi–Ni liquid in the impure (99.5%) Ni. The apparent dihedral angles appeared to be significantly smaller ($\sim 5^\circ$) than those in the pure (99.9945%) Ni (see e.g. Fig. 1a). However, the liquid channels were broken during the solidification and the tips were further smeared by the e-beam irradiation in SEM, making accurate measurements of the dihedral angles difficult.

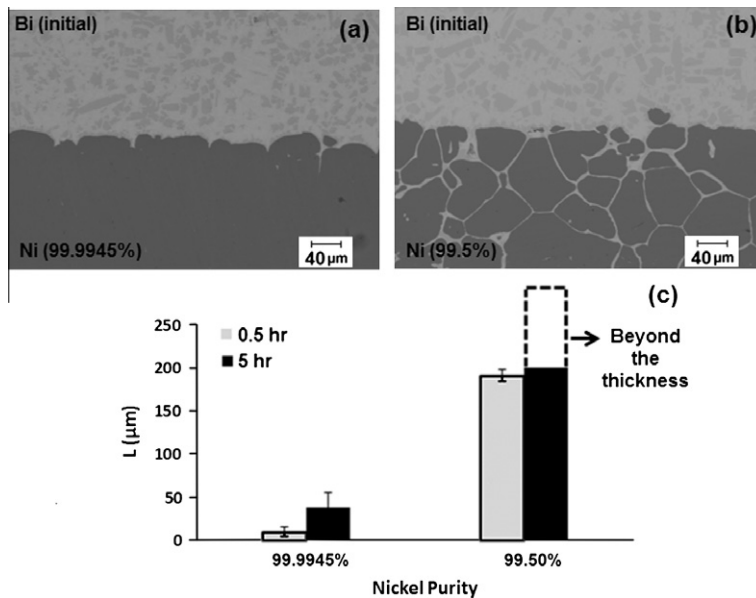


Fig. 6. The effect of the purity of the Ni specimen on the intergranular penetration was even more significant when the Ni specimens were brought into contact with initially pure Bi liquids. SEM cross-sectional images of (a) a pure (99.9945% Ni) specimen and (b) an impure specimen (99.5% Ni, 0.21% Mn, 0.14% Fe and 0.1% Si) of similar average grain sizes of $\sim 75 \mu\text{m}$ after annealing in contact with initially pure Bi liquids at 700°C for 5 h. (c) The measured average penetration lengths for pure and impure Ni foils after annealing in contact with initially pure Bi liquids at 700°C for different durations.

liquid significantly changed the GB wetting and intergranular penetration behaviors in pure Ni foils. The effects of adding 1 at.% and 5 wt.%, respectively, of these three impurities to the 1Bi–0.36Ni liquid on the measured average penetration lengths are shown in a bar chart in Fig. 9 and listed in Table 1. Moreover, the morphologies and kinetics of the intergranular penetration were different in each of the three cases (Fig. 7), as will be discussed in Section 4.4.

First, for specimens annealed at 700°C for 5 h, the addition of 1 at.% Mn to the 1Bi–0.36Ni liquid (to form 0.1Bi–0.36Ni–0.014Mn) resulted in an increase in the liquid penetration length of ~ 3 -fold, from 31 and $95 \mu\text{m}$ (Fig. 8a vs. c); adding a large amount of Mn (5 wt.% Mn, i.e. 1Bi–0.36Ni–0.21Mn) resulted in a more pronounced increase in the penetration length of ~ 17 -fold (to $524 \mu\text{m}$; Fig. 8d). These results indicate that in this system the liquid penetration length depended on the amount of Mn added.

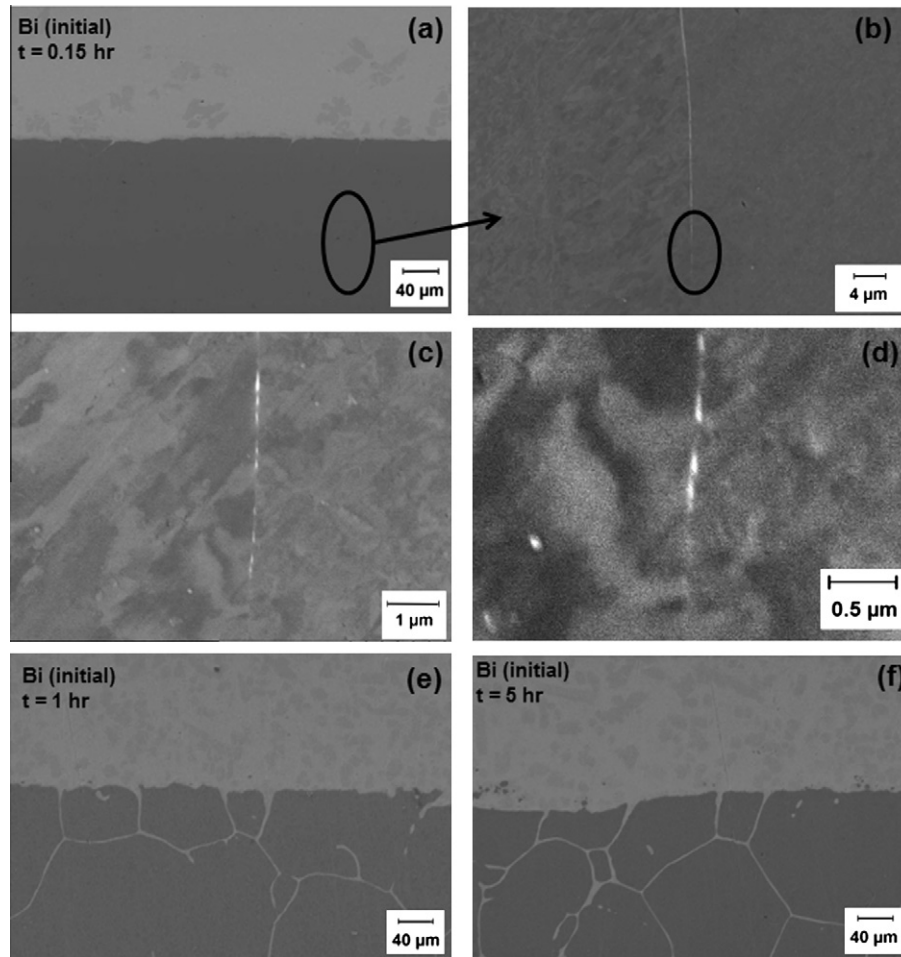


Fig. 7. The time evolution of the intergranular liquid penetration in the impure (99.5% Ni, 0.21% Mn, 0.14% Fe and 0.1% Si) specimens after being brought into contact with initially pure Bi liquids and annealed at 700 °C for (a)–(d) 0.15 h, (e) 1 h and (f) 5 h, respectively. In (c) and (d), Bi-based penetration tips were presumably broken during solidification and probably further smeared by the e-beam irradiation in SEM.

The effect of time on the penetration of the pure Ni with 5 wt.% Mn in the liquid (1Bi–0.36Ni–0.21Mn) is shown in Fig. 10, which illustrates that the liquid penetration was more significant in the early stage. The EDX investigation of the quenched specimens with different amounts of Mn added to the liquid also revealed interesting features. As shown in Fig. 11, after annealing at 700 °C for 5 h, the Bi-based liquid (which was solidified in quenched specimens) no longer contains a significant amount of Mn (<1%); Mn was rejected from the liquid and diffused into the Ni grains. The concentration of Mn in Ni grains was higher in the areas near the bulk liquid, indicating a diffusion process.

Second, the addition of 1 at.% Sn to the 1Bi–0.36Ni liquid resulted in an ~11-fold increase in the liquid penetration length, from 31 to 338 μm, for specimens annealed at 700 °C for 5 h (Fig. 8a vs. f). This enhancement effect was more significant than that after adding the same amount of Mn. However, unlike the case for Mn, adding a large amount of Sn (5 wt.% Sn, i.e. 1Bi–0.36Ni–0.10Sn) did not result in any further significant increase in the penetration length; it only increased slightly, from 338 μm with the addition of 1 at.% Sn to 380 μm with the addition of

5 wt.% (6.7 at.%) Sn (Fig. 8f vs. g; Fig. 9). The origin of this difference in the concentration dependence of the impurity effect for adding Mn vs. Sn will be explained in Section 4.4. Similar to the case of adding Mn, an EDX analysis also showed the rejection of Sn from Bi-based liquid and diffusion of Sn into solid Ni grains (Fig. 12). Furthermore, Ni₃Sn precipitates were also found in the liquid region (e.g. point B in Fig. 12; we measured eight precipitates, all of which had compositions of 25 at.% Sn–75 at.% Ni, with errors of ~±1 at.%).

Finally, the addition of 1 at.% Fe to the 1Bi–0.36Ni liquid resulted in an ~10-fold increase in the liquid penetration length, from 31 to 292 μm, and adding a large amount of Fe (5 wt.% Fe, i.e. 1Bi–0.36Ni–0.21Fe) further increased the penetration length slightly to 337 μm (Fig. 8a vs. i vs. j; Fig. 9). The measured penetration lengths in both cases were similar to the cases of adding Sn; however, the intergranular penetration morphologies were different; in particular, the solid–liquid interfaces were rough (Fig. 13a). An EDX analysis (Fig. 13) revealed that the liquid did not contain any detectable amount of Fe and the added Fe impurity formed Fe–Ni solid solution precip-

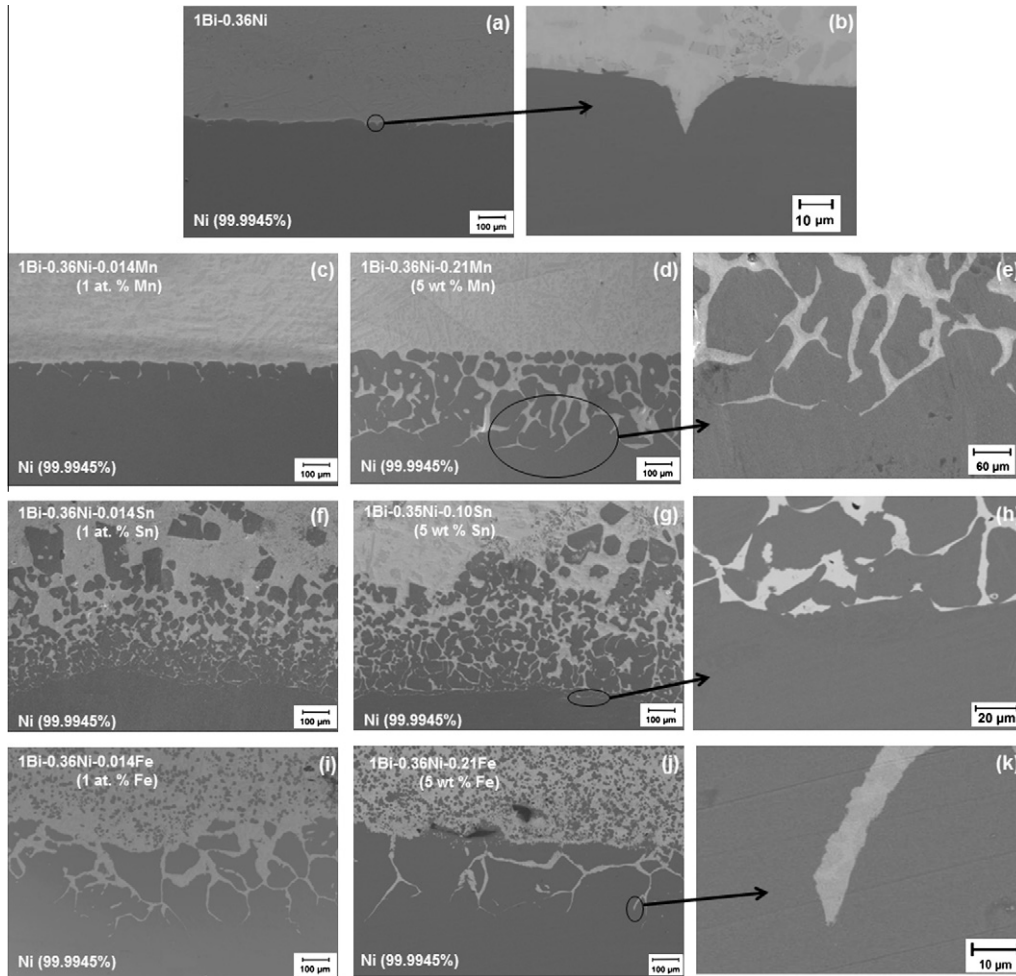


Fig. 8. The effects of the addition of impurities in the liquid on the intergranular penetration of pure (99.9945%) Ni. Representative cross-sectional SEM images for specimens penetrated by (a) and (b) a Bi + 0.36Ni liquid without other impurities (as the reference) vs. Bi–0.36Ni liquids with the addition of different amounts of (c)–(e) Mn, (f)–(h) Sn and (i)–(k) Fe, respectively. The initial liquid compositions are labeled. All specimens were annealed at 700 °C for 5 h.

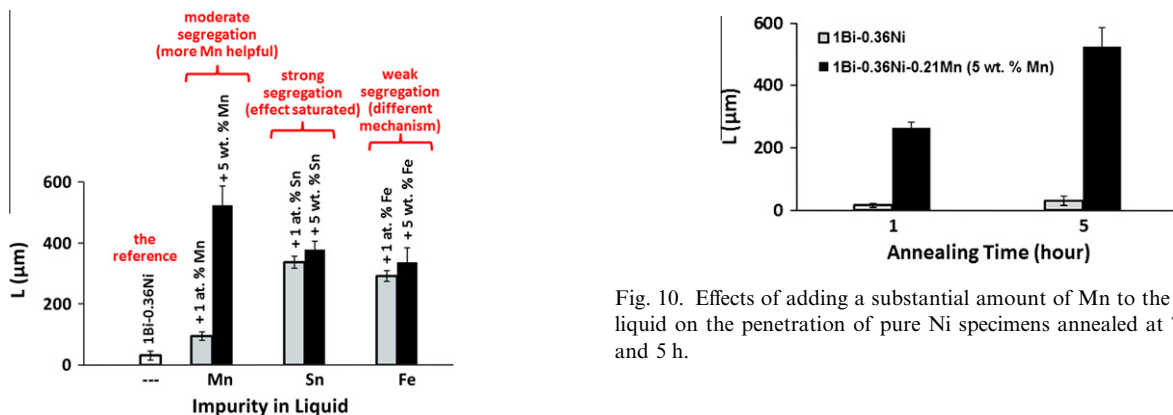


Fig. 9. Effects of the impurity addition in the Bi–Ni liquid on the penetration length in the pure (99.9945%) Ni specimens after annealing at 700 °C for 5 h. Representative SEM images are shown in Fig. 8. The causes for the different behaviors observed are discussed in Section 4.4.

itates. The underlying thermodynamics and kinetics that led to the formation of this different morphology/microstructure will be discussed in Section 4.4.

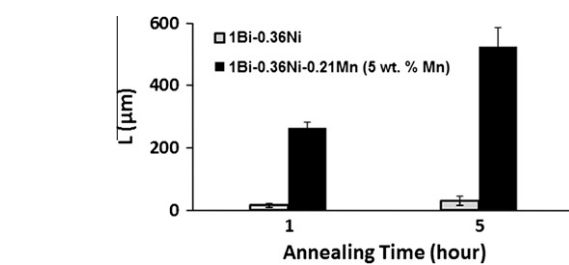


Fig. 10. Effects of adding a substantial amount of Mn to the 1Bi–0.36 Ni liquid on the penetration of pure Ni specimens annealed at 700 °C for 1 and 5 h.

4. Discussion

4.1. Intergranular penetration in the Ni–Bi binary system

Let us first discuss the GB wetting in the Ni–Bi binary system. Using a Miedema-type “macroscopic atom” model that were formulated by Benedictus et al. [42,43] and modified by Shi and Luo (to consider a reference state set by the

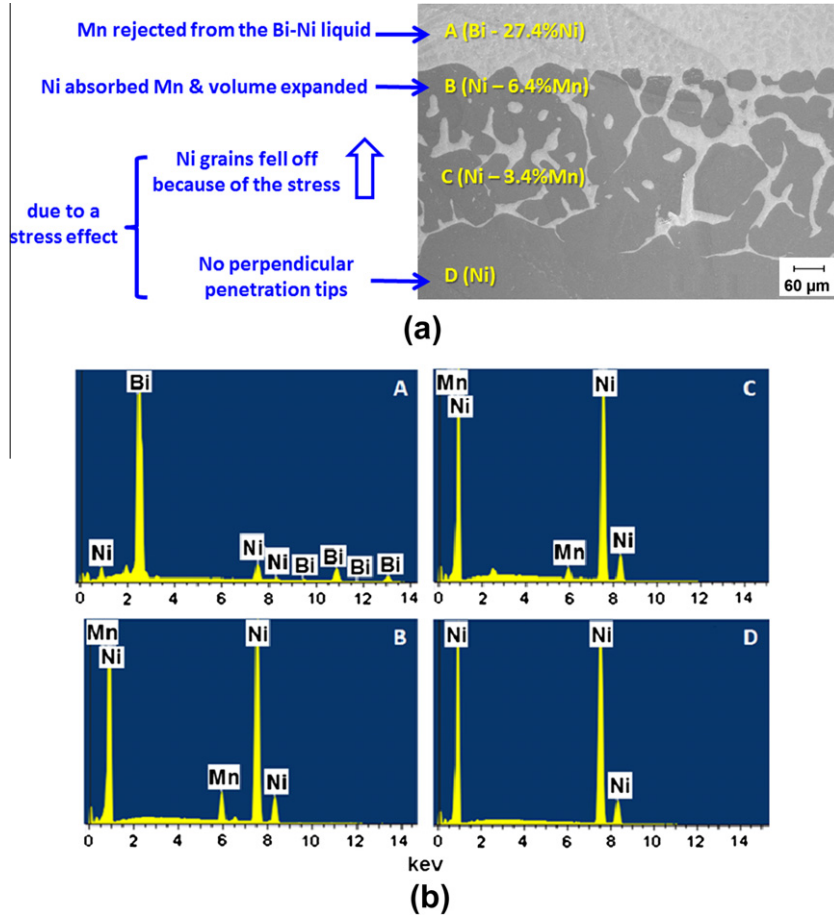


Fig. 11. (a) A representative cross-sectional SEM micrograph of the intergranular penetration of a pure Ni specimen by a Bi–0.36Ni–0.20Mn liquid at 700 °C for 5 h. (b) EDX spectra of four selected regions in (a). See discussion in Section 4.4.

binary liquid) [32], the solid–liquid interfacial energy for the interface between the solid Ni and the equilibrium 1Bi–0.36Ni liquid (i.e. 73.5 at.% Bi + 26.5 at.% Ni) is estimated as:

$$\gamma_{SL} \approx \frac{H_{Ni}^{fuse}}{C_0 V_{Ni}^{2/3}} + \frac{\Delta H_{Ni \text{ in Bi}}^{interface} (F_{Bi}^{Ni})^2}{C_0 V_{Ni}^{2/3}} + \frac{1.9RT}{C_0 V_{Ni/Bi}^{2/3}} \quad (1)$$

(Enthalpic) (Interaction) (Entropic)

$= 0.12 \text{ J m}^{-2}$,

where H_{Ni}^{fuse} is the fusion enthalpy of Ni, $\Delta H_{Ni \text{ in Bi}}^{interface}$ is the enthalpy of solution of Ni in Bi, $C_0 \approx 4.5 \times 10^8$, V is the molar volume, R is the gas constant and F_{Bi}^{Ni} represents the “area” fraction Ni–Bi bonds at the interface defined in Refs. [32,42,43]. The above equation assumes, for simplicity, no near-interface adsorption and ordering. The average excess free energy for a “clean” Ni GB (without any adsorption) can be estimated as [32]:

$$\gamma_{GB}^{(Ni,0)} \approx \frac{1}{3} \gamma_{Ni}^{surface} = \frac{1}{3} \cdot \frac{H_{Ni}^{vap}}{C_0 V_{Ni}^{2/3}} = 0.82 \text{ J m}^{-2} \quad (2)$$

The above value is close to the experimentally estimated average GB energy of 0.92 J m^{-2} (at 700 °C) for a 99.999 wt.% pure Ni [44]. Since

$$\gamma_{GB}^{(Ni,0)} > 2 \cdot \gamma_{SL} \quad (3)$$

complete wetting might (though in reality did not) occur at GBs. It is important to point out that Eq. (3) is a necessary though not sufficient condition for complete GB wetting to occur (since there is significant confusion on this wetting condition in the literature). This is because that the Gibbs adsorption theory tells us that, at a chemical equilibrium, the adsorption of the liquid element (Bi) can significantly reduce the actual (equilibrium) GB energy:

$$\gamma_{GB}^{(Ni-Bi,eq.)} < \gamma_{GB}^{Ni,0} \quad (4)$$

For a case of complete GB wetting, a GB is replaced by two solid–liquid interfaces; thus, if complete GB wetting occurred, we would have $\gamma_{GB}^{(Ni-Bi,eq.)} \equiv 2\gamma_{SL}$ by definition. However, in this case, the observation in Fig. 1a clearly shows that complete GB wetting did not occur. The average equilibrium GB energy (for general GBs with Bi adsorption at the saturated levels, where the bulk chemical potential was defined by the equilibrium 1Bi–0.36Ni liquid) can be estimated by the Young equation:

$$\gamma_{GB}^{(Ni-Bi,eq.)} = 2\gamma_{SL} \cdot \cos\left(\frac{\theta_0}{2}\right) \approx 0.22 \text{ J m}^{-2} \quad (5)$$

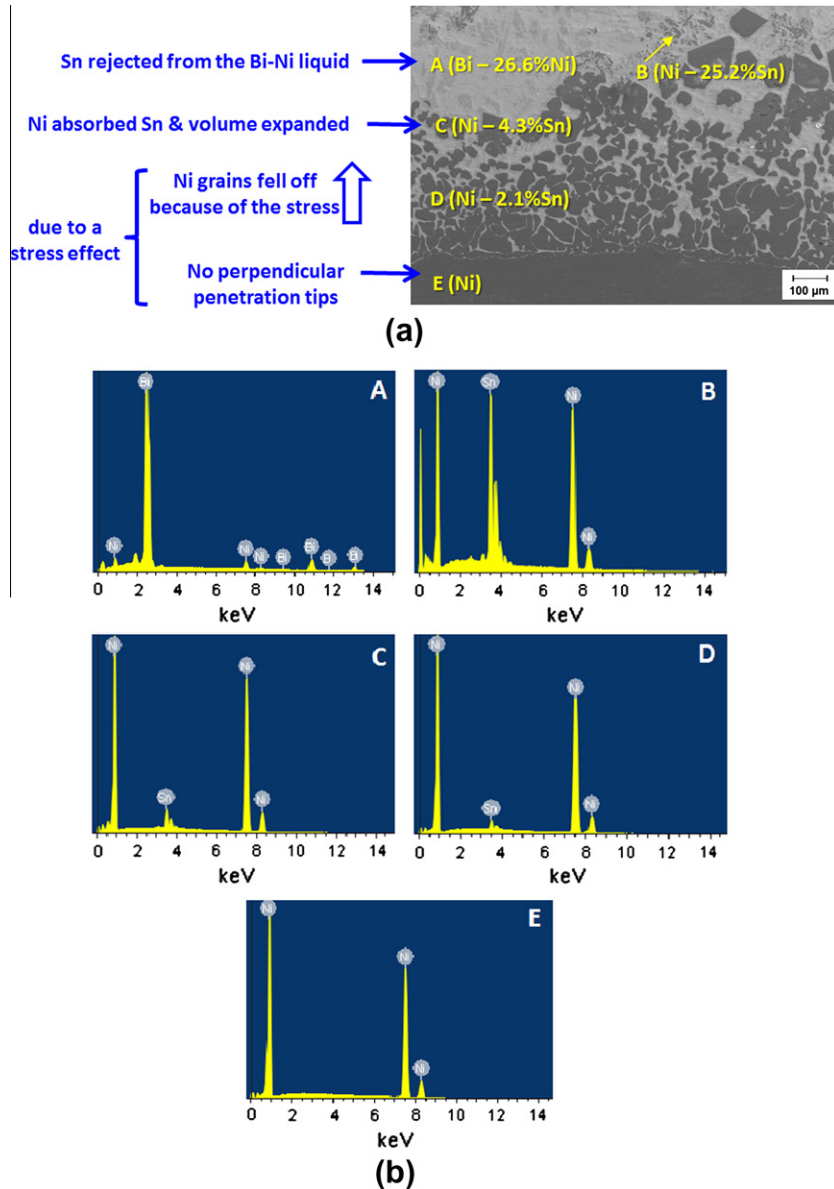


Fig. 12. (a) A representative cross-sectional SEM micrograph of the intergranular penetration of a pure Ni specimen by a Bi–0.36Ni–0.10Sn liquid at 700 °C for 5 h. (b) EDX spectra of five selected regions in (a). See discussion in Section 4.4.

Here, we assume that the average dihedral angle of 44.7° in the Ni–Bi system, where the intergranular penetration was not “finger like” as shown in Fig. 1a, represents the equilibrium (instead of the dynamic) dihedral angle (see discussion below [45]). Although the above estimates may not be very precise (because the Miedema-type models are generally more accurate for cases where both elements are transition metals), they indicate that the adsorption of Bi at GBs significantly reduced the GB energy. This is consistent with the recent observation (using aberration-corrected HAADF STEM) that bilayer adsorption of Bi occurs at all general GBs in front of the liquid penetration tips [30]; this high level of adsorption should lead to a great reduction in GB energy according to the Gibbs adsorption theory.

Several models have been proposed for intergranular liquid penetration in a polycrystalline solid. A classical

model treated intergranular penetration as an analogy to thermal grooving and extended the Mullins model [46,47] by replacing the vapor phase with a liquid phase. This model assumes that the material transport is driven by capillary forces and controlled by diffusion in the liquid phase, and ignores the effects of GB diffusion. The time-dependent groove (penetration) length, L , is given by:

$$L = (1.01 \cot \theta / 2) [D_L \gamma_{SL} C_{\infty L} \Omega^2 / k_B T]^{1/3} t^{1/3}, \quad (6)$$

where D_L is the bulk diffusivity of the solid element in the liquid metal, $C_{\infty L}$ is the solubility of the solid element in the liquid metal, γ_{SL} is the solid–liquid interfacial energy, θ is the dihedral angle, k_B is the Boltzmann constant, T is temperature, Ω is the atomic volume and t is time. Vogel and Ratke [48,49] pointed out that the shapes of experimentally observed intergranular penetration channels can

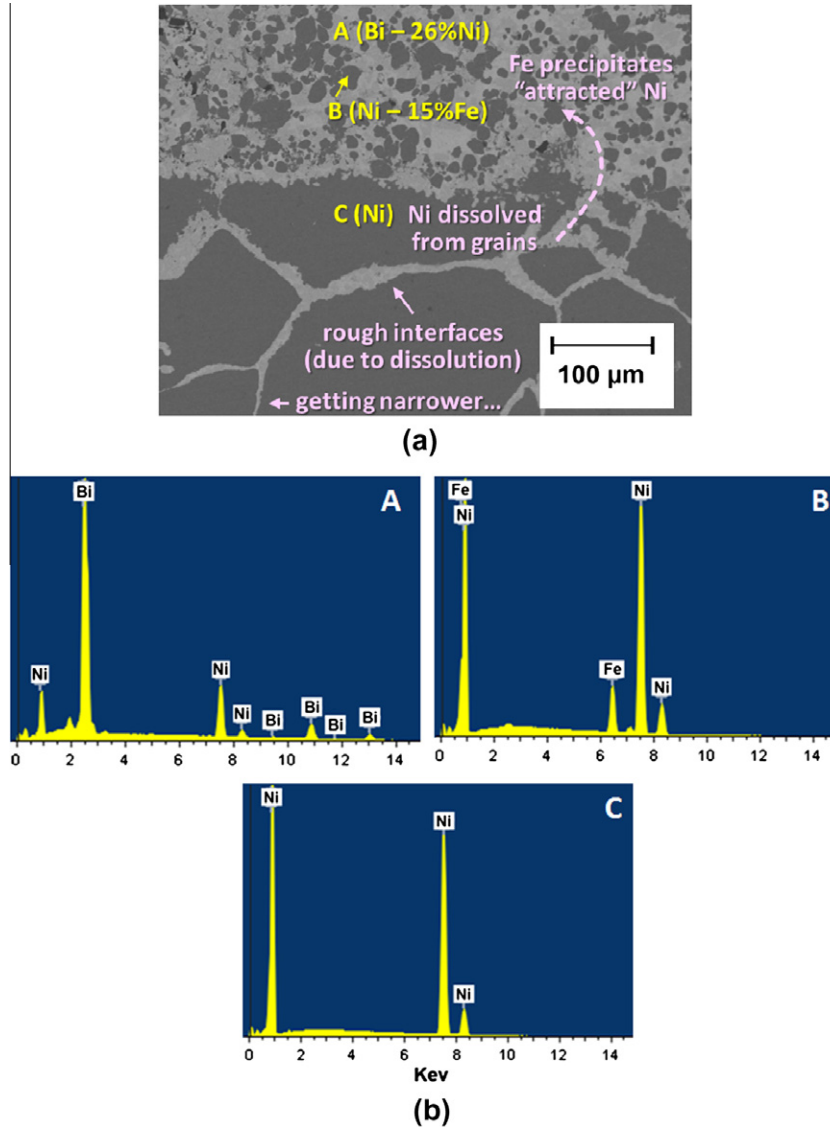


Fig. 13. (a) A representative cross-sectional SEM micrograph of the intergranular penetration of a pure Ni specimen by a Bi–0.36Ni–0.20Fe liquid at 700 °C for 5 h. (b) EDX spectra of three selected regions in (a). See discussion in Section 4.4.

be different from the Mullins-type grooves, and they developed an improved numerical model to consider the effects of GB diffusion. Rabkin [50] proposed that a coherency strain could be responsible for the formation of non-Mullins grooving morphology or the so-called “finger-like” penetration channels; more recently, Klinger and Rabin demonstrated that the dependence of GB energy on composition and the Kirkendall effect during GB interdiffusion could generate tensile stresses that facilitate rapid intergranular penetration as well as intergranular fracture [51,52]. Glickman and Nathan [45] proposed that “finger-like” intergranular penetration resulted from a mechanical inequilibrium at the penetration tip (triple line), where the dihedral angle could not achieve its equilibrium value when the equilibrium dihedral angle approached to zero ($\theta_0 \rightarrow 0$); thus, a dynamic dihedral angle ($\theta_d > \theta_0$) developed. In this model, the imbalance force at the penetration

tip causes stress-driven GB self-diffusion, and the time-dependent penetration length is expressed as:

$$L = \left\{ (\gamma_{gb})^2 \left[1 - \frac{\cos(\theta_d/2)}{\cos(\theta_0/2)} \right]^2 \Omega / D_L \gamma_{SL} C_{\infty L} Z^2 K T \right\} (D_{gb})^2 t, \quad (7)$$

where Z is the characteristic distance between dislocations.

The grooves observed in this study in the Ni–Bi binary system (in the “pure” binary system) were Mullins like. A typical groove is shown in Fig. 1a. A linear fitting of the double logarithmical plot of the penetration length vs. time produced an exponent of $n \approx 0.6$ ($L \propto t^n$). This fitted exponent was between those predicted by the Mullins model ($n = 0.33$) and by the Glickman–Nathan model ($n = 1$). Thus, some significant GB diffusion would likely have occurred and modified the classical Mullins behavior.

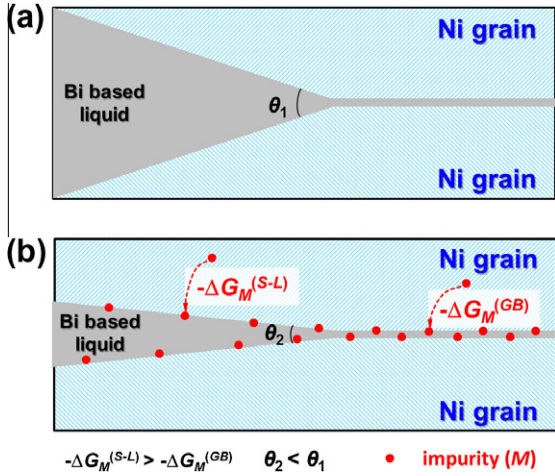


Fig. 14. Schematic illustration of the proposed mechanism for the observed impurity enhanced the intergranular penetration.

There are limited data on the kinetics of grooving in literature for this system; the reported exponent varied from 1 (linear) [53] to 0.5 (parabolic) [54] and 0.2 [1]. Specifically, a recent study [1] conducted on the same system at the same temperature gave an exponent of ~ 0.2 . This difference might have resulted from a relatively higher impurity level of C of the Ni used in that experiment [1]. We should also recognize that the penetration kinetics could be different in the multiple-grain region when the penetration length exceeds one grain size ($\sim 75 \mu\text{m}$). However, the penetration length vs. time curve shown in Fig. 1d does not exhibit a significant change in the kinetic exponent.

4.2. Impurity effects on intergranular penetration in the dilute solution limit

Perhaps the most noteworthy observation of the present study is the significant impurity effects on enhancing the intergranular penetration. Here, we propose to explain this impurity effect based on the assumption that adsorption of an impurity can reduce the solid–liquid interfacial energy faster than the GB energy because the segregation energy is generally more negative at the solid–liquid interface; this proposed mechanism is schematically illustrated in Fig. 14 and is elaborated on below. Note that this concept in our model follows a similar idea to that proposed in the Rice–Wang model [55] for GB embrittlement, that the reduction in GB cohesion is because the surface segregation energy is greater (more negative in the convention used below) than the GB segregation energy. In a recent article [56], Glickman also used a somewhat similar mechanism to explain the “alloying effect” in enhancing stress corrosion cracking in liquid metals or aqueous solutions (by arguing that an alloying element is “a strong surfactant” that reduces the γ_{SL} [56]).

Here, we derive the relevant equations based on the Guttman-type adsorption theory for the dilute solution limit and illustrate the basic underlying concepts (noting

that our specific case is different from the Rice–Wang model for GB embrittlement [55] or the stress corrosion cracking model [56], so we cannot adopt those derivations/analyses directly). When a third impurity, M (such as Mn, Fe or Sn), is present in the Ni–Bi binary system, it will be adsorbed (segregate) at both GBs and solid–liquid interfaces. Let us first consider the dilute solution limit where the amount of M is small, so that it does not cause an interfacial structural transition and the number of the interfacial (GB) adsorption sites can be considered as fixed. Applying the Guttman model for the adsorption of M at the solid–liquid (S–L) interface in the Ni–Bi– M ternary system gives [57]:

$$\frac{X_M^{(\text{S-L})}}{X_{\text{Ni}}^{(\text{S-L})}} = \frac{X_M^{(\text{solid})}}{X_{\text{Ni}}^{(\text{solid})}} \cdot e^{-\frac{-\Delta G_M^{(\text{S-L})}}{kT}} \approx X_M^{(\text{solid})} \cdot \frac{-\Delta G_M^{(\text{S-L})}}{kT} \quad (8)$$

where $X_A^{(\text{location})}$ is the atomic fraction of A ($A = \text{Ni}, \text{Bi}$ or M) in “(location)”, where “(location)” can be “solid”, “solid–liquid (S–L) interface” or “GB”. At the dilute solution limit, $X_M^{(\text{solid})} \ll 1$ and $X_M^{(\text{solid})} \approx 1$; thus, the adsorption (segregation) free energy ($\Delta G_M^{(\text{S-L})} = \Delta G_M^{(\text{S-L},0)} - \alpha X_{\text{Bi}}^{(\text{S-L})}$, where α is a parameter characterizing the dependence of adsorption energy on the interfacial composition) can be considered as a constant ($X_{\text{Bi}}^{(\text{S-L})} \approx \text{constant}$). Note that $\Delta G_M^{(\text{S-L})}$ is negative for the case where M is enriched at the interface in the current definition [57].

The solid–liquid interfacial energy will decrease with the adsorption of M according to the Gibbs adsorption isotherm:

$$\begin{aligned} d\gamma_{\text{SL}} &\approx -\Gamma_M d\mu_M \approx -\Gamma_M kT d \left[\ln \left(X_M^{(\text{solid})} \right) \right] \\ &\approx -\Gamma_0^{(\text{S-L})} X_M^{(\text{S-L})} kT \frac{dX_M^{(\text{solid})}}{X_M^{(\text{solid})}}, \end{aligned} \quad (9)$$

We assume here that the dilute solution follows Henry’s law ($\mu_M = kT \ln(KX_M^{(\text{solid})})$, where K is a constant). $\Gamma_0^{(\text{S-L})}$ is the number of adsorption sites at the solid–liquid interfacial phase ($\Gamma_M \approx \Gamma_0^{(\text{S-L})} X_M^{(\text{S-L})}$, assuming that $\Gamma_0^{(\text{S-L})}$ is roughly a constant and the molar fractions of M in the bulk phases are negligible). Combining Eqs. (8) and (9) produces:

$$\left. \frac{d\gamma_{\text{SL}}}{dX_M^{(\text{solid})}} \right|_{X_M^{(\text{solid})} \rightarrow 0} = -\Gamma_0^{(\text{S-L})} X_{\text{Ni}}^{(\text{S-L})} kT \cdot e^{-\frac{-\Delta G_M^{(\text{S-L})}}{kT}}. \quad (10)$$

Similarly, we can derive the following equation for the impurity effect on changing GB energy for the dilute solution limit:

$$\left. \frac{d\gamma_{\text{GB}}}{dX_M^{(\text{solid})}} \right|_{X_M^{(\text{solid})} \rightarrow 0} = -\Gamma_0^{(\text{GB})} X_{\text{Ni}}^{(\text{GB})} kT \cdot e^{-\frac{-\Delta G_M^{(\text{GB})}}{kT}}. \quad (11)$$

The equilibrium dihedral angle is defined by the Young equation:

$$\cos \left(\frac{\theta_0}{2} \right) = \frac{\gamma_{\text{GB}}}{2 \cdot \gamma_{\text{SL}}}. \quad (12)$$

Differentiating Eq. (12) and incorporating Eqs. (10) and (11) gives:

$$\begin{aligned} & \left. \frac{d\theta_0}{dX_M^{(\text{solid})}} \right|_{X_M^{(\text{solid})} \rightarrow 0} \\ &= \left\{ \frac{1}{\sin(\theta_0/2) \cdot \gamma_{\text{SL}}} \left[-\frac{d\gamma_{\text{GB}}}{dX_M^{(\text{solid})}} + 2\cos\left(\frac{\theta_0}{2}\right) \frac{d\gamma_{\text{SL}}}{dX_M^{(\text{solid})}} \right] \right\} \bigg|_{X_M^{(\text{solid})} \rightarrow 0} \\ &= \frac{kT}{\sin(\theta_0/2) \cdot \gamma_{\text{SL}}^{(X_M^{(\text{solid})}=0)}} \left[\Gamma_0^{(\text{GB})} X_{\text{Ni}}^{(\text{GB})} \cdot e^{-\frac{\Delta G_M^{(\text{GB})}}{kT}} \right. \\ & \quad \left. - 2\cos\left(\frac{\theta_0}{2}\right) \Gamma_0^{(\text{S-L})} X_{\text{Ni}}^{(\text{S-L})} \cdot e^{-\frac{\Delta G_M^{(\text{S-L})}}{kT}} \right] \end{aligned} \quad (13)$$

The above equation can be rewritten as:

$$\left. \frac{d\theta_0}{dX_M^{(\text{solid})}} \right|_{X_M^{(\text{solid})} \rightarrow 0} = \beta_1 \cdot \left\{ 1 - \beta_2 \cdot e^{-\frac{[-G_M^{(\text{S-L})}] - [-G_M^{(\text{GB})}]}{kT}} \right\}, \quad (14)$$

where

$$\beta_1 \equiv \frac{kT \cdot \Gamma_0^{(\text{GB})} X_{\text{Ni}}^{(\text{GB})} \cdot e^{-\frac{\Delta G_M^{(\text{GB})}}{kT}}}{\sin(\theta_0/2) \cdot \gamma_{\text{SL}}^{(X_M^{(\text{solid})}=0)}} \quad (15)$$

and

$$\beta_2 \equiv \cos\left(\frac{\theta_0}{2}\right) \cdot \frac{2\Gamma_0^{(\text{S-L})}}{\Gamma_0^{(\text{GB})}} \cdot \frac{X_{\text{Ni}}^{(\text{S-L})}}{X_{\text{Ni}}^{(\text{GB})}} \quad (16)$$

are two parameters. Since β_2 is a dimensionless number on the order of one, the equilibrium dihedral angle will decrease with the addition of a small amount of M if the segregation free energy is significantly more negative at the solid–liquid interface than the GB (i.e. $\{[-\Delta G_M^{(\text{S-L})}] - [-\Delta G_M^{(\text{GB})}]\}/(kT)$ is a significant positive number; again, note that in this definition ΔG is negative for a case of positive interfacial segregation).

In an analogous case of GB embrittlement (reduction in GB cohesion by impurity adsorption/segregation), Rice and Wang [55] showed that, for most (but not all) cases, $\{[-\Delta G_M^{(\text{surface})}] - [-\Delta G_M^{(\text{GB})}]\}$ is positive and significant (around 50–100 kJ mol⁻¹ for many cases, i.e. $\{[-\Delta G_M^{(\text{surface})}] - [-\Delta G_M^{(\text{GB})}]\}/(kT)$ is in the range of 6–12 at $T = 1000$ K). Rice and Wang also explained the origin of GB embrittlement based on the fact that $[-\Delta G_M^{(\text{surface})}]$ is generally greater than $[-\Delta G_M^{(\text{GB})}]$, so the segregation will reduce the surface energy more than the GB energy, which in turn will reduce the cohesion energy.

In the current case, there are no experimental data or reliable models to estimate the segregation energy of a third impurity (such as Mn, Sn and Fe) in the Ni–Bi– M ternary systems. Our experiments have shown that, in the impure Ni, the apparent average dihedral angle reduced from $\sim 44.7^\circ$ to $\sim 5^\circ$, as shown in Figs. 5 and 7c and d. This reduction in the dihedral angle suggests that $[-\Delta G_M^{(\text{S-L})}]$ is also greater than $[-\Delta G_M^{(\text{GB})}]$. A prior study [30] showed that a bilayer adsorption of Bi occurs at general GBs in the Ni–

Bi binary system at 700 °C; hence, the chemical environments of the M segregants should be similar at the GB and solid–liquid interface. However, M segregants might have higher energy states at the GB because of the confinement and the ordering [30], which make it more difficult to relax the strain energy and cause structural frustration. This should lead to a general smaller value of $[-\Delta G_M^{(\text{GB})}]$ than $[-\Delta G_M^{(\text{S-L})}]$ for many (but perhaps not all) impurities, which is analogous to the case of GB embrittlement and the Rice–Wang model. This should reduce the average equilibrium dihedral angle and enhance the intergranular penetration with the impurity addition in general, though exceptions can certainly exist. This proposed mechanism is illustrated schematically in Fig. 14.

Both the Mullins model (Eq. (6)) and the Glickman–Nathan model (Eq. (7)) suggest that a reduction in the equilibrium dihedral angle (θ_0) will increase the intergranular penetration length. Specifically, in the Mullins model, the penetration length would increase by 4.7 and 9.5 times if θ_0 was reduced from ~ 44.7 to 10 and 5° , respectively; this is consistent with our experimental observation of an ~ 6 -fold increase (Fig. 4b), though we should point out that the penetration tips in the impure Ni were more “finger like”, indicating the intergranular penetration may differ from the Mullins model (where the GB diffusion likely contributed substantially). More critical and quantitative assessments of current observations are not feasible at this time.

4.3. Further considerations: interfacial phase (complexion) and GB diffusion

Recent studies have revealed the existence of nanoscale impurity-based GB phases, particularly the “equilibrium-thickness” intergranular films in ceramic materials [26–28,58–62]. More recent studies also uncovered the existence of impurity-based GB phases in binary metallic systems such as W–Ni [31,33,34] and Mo–Ni [32,38,39]. Similar impurity-based interfacial phases have also been found on free surfaces [27,63–68] and at phase boundaries [26,69–75]. A series of other discrete GB “complexions” (i.e. interfacial phases), such as monolayers, bilayers and trilayers, have been observed [18–21,23–25,76]. Specifically, a bilayer interface phase has been ubiquitously observed at general GBs in the Ni–Bi binary system [30].

We should note that the above analysis of the impurity effects on the equilibrium dihedral angle and intergranular penetration was based on the dilute solution limit, where we assume that the amount of the third impurity is so small that it would not induce a transition in the atomic-scale interfacial structure. The presence of a moderate amount of a third impurity can further induce a change in the atomic-scale interfacial structural transition (i.e. a complexion transition), which may lead to more diversified and complex interfacial behaviors than that discussed in the previous section for the dilute solution limit. The observation made in this study will likely simulate future studies

to take on a highly challenging job to seek and characterize such atomic-scale interfacial structural transitions.

In addition to the interfacial energies and the equilibrium dihedral angle (thermodynamic quantities), another factor to consider is that adding impurities can affect the intergranular penetration kinetics by changing the transport rates, particularly the GB diffusivity. A prior study [44] measured the GB diffusivities of a 99.999 wt.% Ni and a 99.96 wt.% Ni (where the four major impurities are Mn, Fe, Cu and Si, being similar to our “impure Ni”), and showed that the presence of these impurities reduced GB diffusivities significantly. This appears to suggest that these impurities should not enhance intergranular penetration via increasing the GB diffusion rates. However, we have to recognize that our case is different because of the presence of a Bi-rich liquid, which induced a GB structural transition that led to the formation of a Bi-based bilayer interfacial phase at all general GBs in the Ni–Bi binary system [30]. The addition of other impurities could further change the interfacial structure and the associated diffusion rates; this will be the subject of a future study.

4.4. Effects of bulk equilibria: dissolution, precipitation, diffusion and stress generation

When the initial liquid used was pure Bi, instead of the equilibrium 1Bi–0.36Ni, the intergranular penetration was more significant. This can be attributed to a dissolution effect, i.e. Ni dissolved from the solid into the Bi-rich liquid until the equilibrium 1Bi–0.36Ni composition was reached. Specifically, when the pure (99.9945 at.%) Ni was used, the application of the initially pure Bi resulted in only a moderate increase in the penetration length (by ~23%) for the annealing time of 5 h. When the impure (99.5 at.% Ni) was used, the application of the initially pure Bi resulted in wider and uniform liquid channels (Fig. 4c vs. Fig. 6b) as well as a much more significant increase in the penetration length (Table 1 and Fig 6c). This difference can be understood from the much smaller dihedral angle (~5°) in the impure (99.5 at.%) Ni; thus, the penetration channels were more “finger like”, with an almost constant width at a particular time, and the channel width grew over time (Fig. 7).

When a third impurity element (Mn, Sn or Fe) was added to the 1Bi–0.36Ni liquid, the intergranular penetration was also significantly increased (Figs. 8 and 9), which was similar to the case where the impurities were present in the solid Ni (Fig. 4). However, the morphologies of the intergranular penetration were different (Fig. 8 vs. Fig. 4). The different intergranular penetration kinetics and morphologies can be fully explained by considering the bulk phase/chemical equilibria (which generate transport processes and stress, as we will discuss subsequently) in conjunction with the segregation effects discussed above. To discuss the relevant microstructural evolutions, we sketch the key features of the 700 °C isothermal sections of the three ternary phase diagrams for Ni–Bi–M

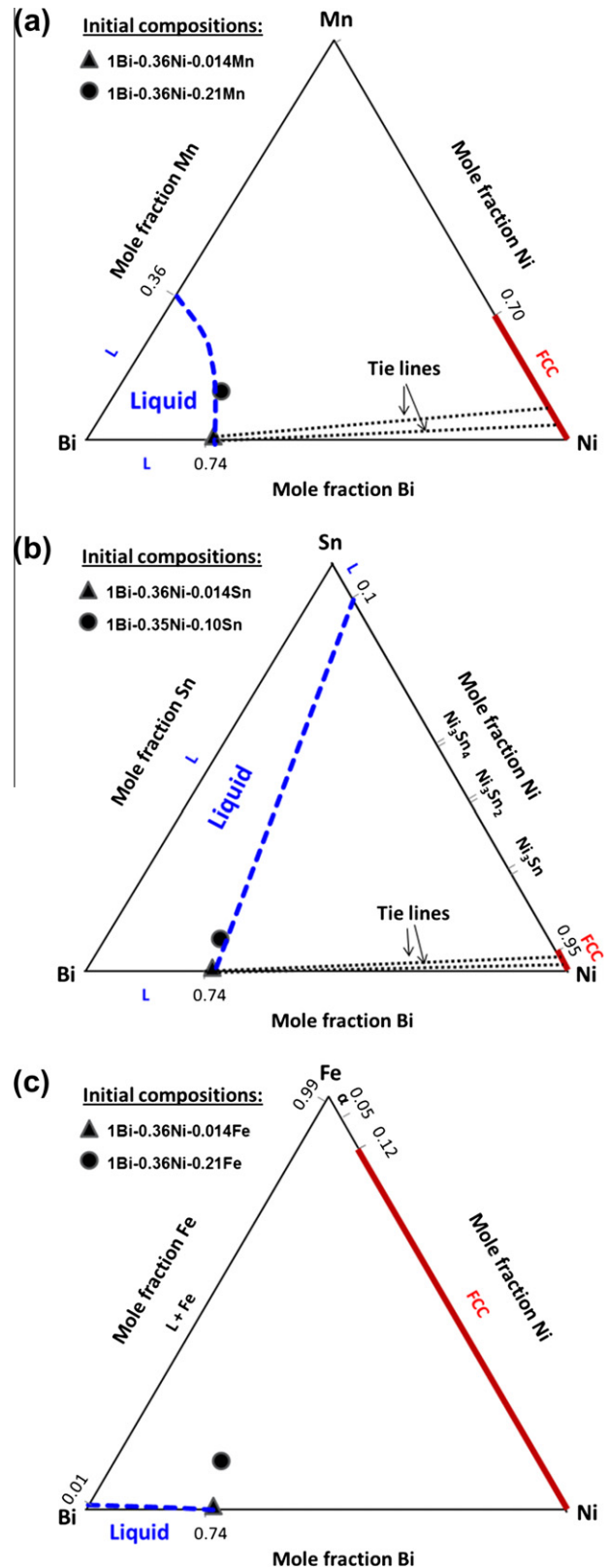


Fig. 15. Schematic sketches of the key features (that are relevant to our experiments) in the isothermal sections of the (a) Bi–Ni–Mn, (b) Bi–Ni–Sn and (c) Bi–Ni–Fe ternary phase diagrams at 700 °C. Liquidus (blue dashed), solidus (red solid) and tie (dotted) lines are also shown. (For interpretation of the references to color in this figure legend, the reader is referred to the web version of this article.)

($M = \text{Mn}, \text{Sn}$ or Fe) in Fig. 15. Note that there are no available measured or computed ternary phase diagrams for these systems; thus, in Fig. 15 we sketch the key features that are relevant to our experiments, i.e. solidus, liquidus and tie lines, based on the binary phase diagrams as well as our experimental observations, such as the SEM–EDX results shown in Figs. 11–13.

Let us first discuss the cases where Mn and Sn were added singly to the liquid, since these two cases exhibited many similarities (though with a key difference in the concentration dependence of the impurity effects, which will be discussed later). As shown in Fig. 15a and b, the Bi–Ni-based liquid has significant solubilities of Mn and Sn (i.e. the ternary liquidus line starts from a Bi–Ni binary composition and ends at a Bi–Mn or Bi–Sn binary composition), while the Ni-based solid face-centered cubic (fcc) phase has only moderate solubility of Mn (up to ~ 30 at.%) and Sn (up to ~ 5 at.%). Somewhat surprisingly, SEM–EDX analyses (Figs. 11 and 12) showed that Mn and Sn were (almost completely) rejected from the Bi–Ni liquid (see points A in Figs. 11 and 12) and dissolved and diffused into the Ni grains (see points B and C in Fig. 11 and points C and D in Fig. 12). These results clearly indicate that, at chemical/phase equilibria, both Mn and Sn tend to partition in the Ni-based solid fcc phase instead of the Bi–Ni-based liquid. Assuming that the Ni-based solid and Bi–Ni-based liquid phases were in local equilibria at the solid–liquid interfaces in Figs. 11 and 12, the corresponding tie lines are labeled in the corresponding ternary phase diagrams in Fig. 15a and b.

The repartitioning of Mn and Sn has two significant implications. First, it implies the existence of a kinetic process (in addition to the intergranular penetration) that has transported the third impurity element (Mn or Sn) from the Bi–Ni-based liquid phase into the solid–liquid interface, where the impurity element has further dissolved and diffused into the Ni-based solid phase. This kinetic process resulted in concentration gradients in the solid Ni phases, which were verified by the SEM–EDX analyses (Figs. 11 and 12). Second, the dissolution of Mn or Sn into the Ni-based solid fcc phase should lead to a volume expansion of the solid phase and should generate compressive stresses/strains. This explains the different intergranular penetration morphologies when Mn or Sn was added into the liquid.

As shown in Figs. 8e and 11a (after adding Mn) and Figs. 8h and 12a (after adding Sn), the “penetration fronts” were parallel to the original specimen surfaces and no penetration tip was perpendicular to the specimen surfaces (in contrast to the morphologies shown in Figs. 1 and 4). Presumably, such morphologies (Figs. 8e and h, 11a and 12a) formed because they could release the compressive stresses generated by the volume expansions associated with the dissolution of Mn or Sn into the solid grains. Note that, in the present case, Mn or Sn dissolved from the liquid phase into the solid Ni grains, but the Ni did not dissolve from the solid back into the liquid phase. This can be

deduced from the phase diagrams in Fig. 15 and verified from the EDX analyses (Figs. 11 and 12); both showed that the Ni/Bi ratio was unchanged, implying no dissolution of Ni from the solid to the liquid phase. Thus, although Mn and Sn are substitutional solutes in Ni, the dissolution and diffusion of Mn or Sn from the liquid phase into the Ni grains resulted in an increase in the solid volume because of an increase in the total amount (number of atoms) of the solid phase, which led to volume expansions of the solid grains. Consequently, solid grains were spalled off. Moreover, possible fast diffusion of impurities along GBs could generate local stresses that further facilitate the precipitation of grains. Finally, the grains precipitated in the liquid phase could be rearranged and organized due to capillary forces, which are shown in Figs. 8e and 11a (after adding Mn) and Figs. 8h and 12a (after adding Sn).

In contrast, in the case of penetrating impure Ni foils with initially pure Bi, uniform intergranular penetration channels (with constant widths) are observed in Fig. 7, which likely resulted from the dissolution of Ni into the liquid, which led to a reduction in the volume of solid Ni grains.

Figs. 8 and 9 also illustrate a key difference in the penetration behavior of Mn vs. Sn when added to the liquid. On the one hand, adding a small amount (1 at.%) of Mn in the liquid enhanced the intergranular penetration only moderately (by 3-fold), while adding a large amount (5 wt.%) enhanced it significantly more (by 17-fold). On the other hand, adding just a small amount (1 at.%) of Sn enhanced the intergranular penetration significantly (by 11-fold), and adding a larger amount (5 wt.%) did not enhance the penetration much further (by 12-fold only). This can be explained from the fact that the solubility limit of Sn in Ni is only ~ 5 at.%, whereas that of Mn in Ni is ~ 30 at.% (Fig. 15). It is well established that the GB enrichment ratio ($\beta_{\text{enrich}} \equiv X_{\text{M}}^{(\text{GB})}/X_{\text{M}}^{(\text{solid})} \approx \exp(-\Delta G_{\text{M}}^{(\text{GB})})$) is inversely proportional to the solid solubility limit [77,78], and a similar relation may also apply for other types of interface. This suggests that the GB and interfacial segregation is only moderate for Mn. Thus, adding a small amount of Mn had only a moderate effect in enhancing the intergranular penetration via a reduction in the equilibrium dihedral angle based on the mechanism proposed in Section 4.2, and adding a greater amount of Mn further enhanced the penetration. In contrast, the enrichment ratios were greater for Sn segregation; thus, adding only a small amount of Sn had a significant effect, and increasing the amount of Sn added did not increase it much further because the segregation level was already close to saturation. Moreover, when the Sn/Ni ratio was above ~ 0.05 , Ni_3Sn particles precipitated (as observed by SEM–EDX; see Fig. 12, point B); this was an additional (presumably secondary) cause for the saturation of the enhancement effect.

Finally, the mechanism for enhancing intergranular penetration via the addition of Fe to the Bi–Ni liquid is somewhat different from the other cases. On the one hand, the

solid solubility limit of Fe in Ni is as large as 88 at.% (Fig. 15c), indicating weak Fe segregation at GBs or interfaces (because β_{enrich} is inversely proportional to the solid solubility limit [77,78]). Thus, the mechanism proposed in Section 4.2 should be less effective. Consistent with this, the average dihedral angle for this case was measured to be 38.7° (with an associated standard deviation of $\sim 11.8^\circ$; Fig. 8k), which was close to the average dihedral angle of 44.7° measured for the Bi–Ni binary system without the addition of Fe. On the other hand, the solubility of Fe in Bi–Ni is very low (Fig. 15c). Thus, when Fe was “added” to the Bi–Ni liquid, it actually precipitated out as solid particles in the liquid. These solid precipitates consumed some Ni from the liquid, resulting in a chemical potential gradient for Ni, which caused some of the Ni from the Ni grains to dissolve in the liquid. The preferential dissolution of solid Ni at GBs enhanced the intergranular penetration. The observation of rough solid–liquid interfaces (Fig. 13a) and the gradual narrowing in the width of the intergranular liquid channels (Figs. 8i, j and 13a) support this proposed mechanism.

5. Concluding remarks

In summary, the effects of adding additional (third and beyond) impurities on the intergranular liquid metal penetration of a solid polycrystalline metal was systematically investigated using Bi–Ni-based systems as models. A framework for understanding such impurity effects was developed. The variety of intergranular penetration kinetics and morphologies observed from our experiments, which used 10 different combinations of solid–liquid couples, could be explained well by the interplay of interfacial segregation and wetting, bulk phase equilibria, dissolution, precipitation and related transport processes, and the stress generation associated with dissolution. The key conclusions are:

- (1) Although $\gamma_{\text{GB}}^{(\text{Ni},0)} > 2\gamma_{\text{SL}}$ (where $\gamma_{\text{GB}}^{(\text{Ni},0)}$ is excess energy for a “clean” GB) in the Ni–Bi binary system, the Bi-rich liquid does not completely wet the Ni GB. This is because the adsorption of Bi significantly reduces the GB energy ($\gamma_{\text{GB}}^{(\text{Ni-Bi,eq.})} < \gamma_{\text{GB}}^{(\text{Ni},0)}$) so that $\gamma_{\text{GB}}^{(\text{Ni-Bi,eq.})} = 2\gamma_{\text{SL}} \cos(\theta_0/2) < 2\gamma_{\text{SL}}$ at the chemical equilibration.
- (2) The presence of minor impurities can significantly enhance the intergranular penetration. For example, <0.5 at.% total impurities in the solid Ni could increase the penetration length by six times when a near-equilibrium Bi–Ni liquid was applied.
- (3) A new analytical model has been derived for the impurity effect on changing the equilibrium dihedral angle (which controls the penetration kinetics) for the dilute solution limit. We recognize that a moderate amount of impurity may further lead to interfacial structural (phase) transitions; therefore, more

complex theories are needed and more complex penetration behaviors are expected beyond the dilute solution limit.

- (4) When the initially pure Bi was applied, the intergranular penetration could be enhanced due to a dissolution effect, and this enhancement could be magnified when it interacts with the impurity effects.
- (5) When Mn or Sn was initially added to the liquid, it was rejected from the liquid and dissolved and diffused into solid Ni grains. In addition to the normal impurity effects, this process generated compressive stresses/strains because of the volume expansions, which led to different intergranular wetting and penetration morphologies.
- (6) The interfacial segregation of Mn is likely moderate. Thus, adding a small amount (1 at.%) of Mn only enhanced intergranular penetration moderately (by 3-fold), while adding a large amount (5 wt.%) of Mn enhanced the penetration significantly more (by 17-fold). In contrast, the interfacial segregation of Sn is likely strong. Consequently, adding a small amount (1 at.%) of Sn enhanced the penetration significantly (by 11-fold), and adding a larger amount (5 wt.%) of Sn did not enhance the penetration much further (by 12-fold only) because the interfacial segregation was already close to the saturation level.
- (7) When Fe was “added” to the Bi–Ni liquid, it precipitated out as solid particles. These solid precipitates consumed some Ni from the liquid and thereby caused some Ni from the Ni grains to dissolve in the liquid. This resulted in a significant enhancement of intergranular penetration, even though the interfacial segregation of Fe is likely weak. This different mechanism resulted in yet another type of morphology, including the rough solid–liquid interfaces and the tapering of the intergranular liquid channels.

The basic concepts, model and framework developed in this study (and summarized above) can be generalized to explain the impurity effects on intergranular liquid metal penetration in polycrystalline solid metals in other materials systems.

Acknowledgements

The authors acknowledge the financial support from the Electron and Scanning Probe Microscopies program in the DOE Office of Basic Energy Science, DMSE (Grant No. DE-FG02-08ER46511, monitored by Dr. J.G. Zhu).

References

- [1] Wolski K, Laporte V. Mater Sci Eng A 2008;495:138.
- [2] Wolski K, Laporte V, Marie N, Biscondi M. Interface Sci 2001;9:183.
- [3] Nam HS, Srolovitz DJ. Phys Rev Lett 2007;99.
- [4] Joseph B, Picat M, Barbier F. Eur Phys J Appl Phys 1999;5:19.
- [5] Zhang J, Li N. J Nucl Mater 2008;373:351.
- [6] Zhang J, Hosemann P, Maloy S. J Nucl Mater 2010;404:82.

- [7] Zhang J, Li N. *Corrosion* 2004;60:331.
- [8] Zhang J, Li N. *Oxidation Metals* 2005;63:353.
- [9] Zhang J, Marcille TF, Kapernick R. *Corrosion* 2008;64:563.
- [10] Marie N, Wolski K, Biscondi M. *Scripta Mater* 2000;43:943.
- [11] Marie N, Wolski K, Biscondi M. *J Nucl Mater* 2001;296:282.
- [12] Pereiro-López E, Ludwig W, Bellet D, Cloetens P, Lemaignan C. *Phys Rev Lett* 2005;95:215501.
- [13] Zhang J. *Corrosion Sci* 2009;51:1207.
- [14] Pereiro-Lopez E, Ludwig W, Bellet D. *Acta Mater* 2004;52:321.
- [15] Pereiro-Lopez E, Ludwig W, Bellet D, Lemaignan C. *Acta Mater* 2006;54:4307.
- [16] Sigle W, Richter G, Ruhle M, Schmidt S. *Appl Phys Lett* 2006;89:121911.
- [17] Sapundjiev D, Van Dyck S, Bogaerts W. *Corrosion Sci* 2005;48:577.
- [18] Dillon SJ, Harmer MP, Luo J. *JOM* 2009;61(12):38.
- [19] Dillon SJ, Tang M, Carter WC, Harmer MP. *Acta Mater* 2007;55:6208.
- [20] Harmer MP. *J Am Ceram Soc* 2010;93:301.
- [21] Harmer MP. *Science* 2011;332:182.
- [22] Tang M, Carter WC, Cannon RM. *Phys Rev B* 2006;73:024102.
- [23] Tang M, Carter WC, Cannon RM. *Phys Rev Lett* 2006;97:075502.
- [24] Luo J. *Appl Phys Lett* 2009;95:071911.
- [25] Dillon SJ, Harmer MP. *J Eur Ceram Soc* 2008;28:1485.
- [26] Baram M, Chatain D, Kaplan WD. *Science* 2011;322:206.
- [27] Luo J. *Crit Rev Solid State Mater Sci* 2007;32:67.
- [28] Luo J. *Curr Opin Solid State Mater Sci* 2008;12:81.
- [29] Straumal BB, Baretzky B. *Interface Sci* 2004;12:147.
- [30] Luo J, Cheng H, Asl KM, Kiely CJ, Harmer MP. *Science* 2011;333:1730.
- [31] Luo J, Shi XM. *Appl Phys Lett* 2008;92:101901.
- [32] Shi X, Luo J. *Phys Rev B* 2011;84:014105.
- [33] Luo J, Gupta VK, Yoon DH, Meyer HM. *Appl Phys Lett* 2005;87:231902.
- [34] Gupta VK, Yoon DH, Meyer III HM, Luo J. *Acta Mater* 2007;55:3131.
- [35] Divinski S, Lohmann M, Herzig C, Straumal B, Baretzky B, Gust W. *Phys Rev B* 2005;71:104104.
- [36] Chang L-S, Rabkin EI, Straumal B, Lejcek P, Hofmann S, Gust W. *Scripta Metall Mater* 1997;37:729.
- [37] Chang LS, Rabkin E, Straumal BB, Baretzky B, Gust W. *Acta Mater* 1999;47:4041.
- [38] Shi X, Luo J. *Appl Phys Lett* 2009;94:251908.
- [39] Shi X, Luo J. *Phys Rev Lett* 2010;105:236102.
- [40] Seo SK, Cho MG, Lee HM. *J Electron Mater* 2007;36:1536.
- [41] Dehoff RT. *Metallography* 1986;19:209.
- [42] Benedictus R, Böttger A, Mittemeijer EJ. *Phys Rev B* 1996;54:9109.
- [43] Jeurgens LPH, Wang ZM, Mittemeijer EJ. *Int J Mater Res* 2009;100:1281.
- [44] Divinski SV, Reglitz G, Wilde G. *Acta Mater* 2010;58:386.
- [45] Glickman EE, Nathan M. *J Appl Phys* 1999;85:3185.
- [46] Mullins WW. *J Appl Phys* 1957;28:333.
- [47] Mullins WW. *Trans Metall Soc AIME* 1960;218:354.
- [48] Ratke L, Vogel HJ. *Acta Metall Mater* 1991;39:915.
- [49] Vogel HJ, Ratke L. *Acta Metall Mater* 1991;39:641.
- [50] Rabkin E. *Scripta Mater* 1998;39:685.
- [51] Klinger L, Rabkin E. *Scripta Mater* 2010;62:918.
- [52] Klinger L, Rabkin E. *Acta Mater* 2011;59:1389.
- [53] Cheney RF, Hochgraf FG, Spencer CW. *Trans AIME* 1961;221:492.
- [54] Bishop GH. *Trans Metall Soc AIME* 1968;242:1343.
- [55] Rice JR, Wang J-S. *Mater Sci Eng* 1989;A107:23.
- [56] Glickman EE. *Metall Mater Trans A* 2011;42A:250.
- [57] Lejcek P, Hofmann S. *Crit Rev Solid State Mater Sci* 1995;20:1.
- [58] Clarke DR. *J Am Ceram Soc* 1987;70:15.
- [59] Clarke DR, Shaw TM, Philipse AP, Horn RG. *J Am Ceram Soc* 1993;76:1201.
- [60] Clarke DR, Thomas G. *J Am Ceram Soc* 1977;60:491.
- [61] Kleebe H-J, Cinibulk MK, Cannon RM, Rühle M. *J Am Ceram Soc* 1993;76:1969.
- [62] Luo J, Wang H, Chiang Y-M. *J Am Ceram Soc* 1999;82:916.
- [63] Qian H, Luo J. *Acta Mater* 2008;56:4702.
- [64] Qian HJ, Luo J. *Appl Phys Lett* 2007;91:061909.
- [65] Luo J, Chiang Y-M. *J Eur Ceram Soc* 1999;19:697.
- [66] Luo J, Chiang Y-M. *Acta Mater* 2000;48:4501.
- [67] Luo J, Chiang Y-M. *Annu Rev Mater Res* 2008;38:227.
- [68] Luo J, Chiang Y-M, Cannon RM. *Langmuir* 2005;21:7358.
- [69] Baram M, Kaplan WD. *J Mater Sci* 2006;41:7775.
- [70] Avishai A, Kaplan WD. *Z Metallkd* 2004;95:266.
- [71] Avishai A, Kaplan WD. *Acta Mater* 2005;53:1571.
- [72] Avishai A, Scheu C, Kaplan WD. *Z Metallkd* 2003;94:272.
- [73] Avishai A, Scheu C, Kaplan WD. *Acta Mater* 2005;53:1559.
- [74] Scheu C, Dehm G, Kaplan WD. *J Am Ceram Soc* 2001;84:623.
- [75] Ackler HD, Chiang Y-M. *J Am Ceram Soc* 1997;80:1893.
- [76] Dillon SJ, Harmer MP. *Acta Mater* 2007;55:5247.
- [77] Hondros ED, Seah MP. *Metall Trans* 1977;8A:1363.
- [78] Seah MP. *J Phys F: Metal Phys* 1980;10:1043.